

RESEARCH ARTICLE

10.1002/2015JC010715

Key Points:

- Intensified upwelling forms from a submerged valley
- The upwelling is driven by pressure gradient force (PGF)
- The PGF is induced by both bottom stress curl and vortex squeezing

Correspondence to:

J. Gan,
magan@ust.hk

Citation:

Liu, Z., and J. Gan (2015), Upwelling induced by the frictional stress curl and vertical squeezing of the vortex tube over a submerged valley in the East China Sea, *J. Geophys. Res. Oceans*, 120, 2571–2587, doi:10.1002/2015JC010715.

Received 9 JAN 2015

Accepted 10 MAR 2015

Accepted article online 16 MAR 2015

Published online 2 APR 2015

Upwelling induced by the frictional stress curl and vertical squeezing of the vortex tube over a submerged valley in the East China Sea

Zhiqiang Liu¹ and Jianping Gan¹

¹Department of Mathematics and Division of Environment, Hong Kong University of Science and Technology, Kowloon, Hong Kong

Abstract We conducted a process-oriented modeling study to investigate the characteristics and dynamics of the prominent upwelling over a vast submerged valley in the East China Sea (ECS). The valley is inversely funnel-shaped with the west bank and the east bank oriented in the north-south direction. A cross-bank upward transport occurred along the west bank. It intensified northward and peaked around the head of the valley. An along-bank southward pressure gradient force (PGF) formed the cross-bank geostrophic transport for the upwelling over the valley. The PGF reached its maxima at the head of the valley. Our momentum and vorticity dynamic analyses revealed that a bottom stress curl mainly contributed the PGF along the west bank. At the same time, both the bottom stress curl and the nonlinear vorticity advection contributed to the PGF around the head. The bottom stress curl was due to the bottom shear vorticity of the coastal current and the curvature vorticity around the head. The nonlinear vorticity advection formed because of the vertical squeezing of vortex tube as the current flowed over the valley. The nonlinearity mainly affected the PGF around the head, whereas the bottom stress curl contributed to the PGF over the entire valley. The ratio of the nonlinear to frictional contributions to the PGF increased as the coastal current intensified. Our study demonstrates that the PGF that drives the upwelling over the valley is the combined result of the nonlinearity due to vertical squeezing of vortex tube and bottom frictional effects.

1. Introduction

We conducted a modeling study of the variable summer upwelling in the East China Sea (ECS) to investigate the processes and dynamics that govern the response of wind-driven circulation to a distinct, seaward widening, and submerged valley (dashed box in Figure 1). This submerged valley is located in the central part of the northwest ECS off the Changjiang Estuary (CJE). A shallow (<50 m) and vast submarine delta borders the valley to the northeast, off the Jiangsu coast (Subei Shoal, Figure 1). The 50 m isobath forms the boundary of the submerged valley and is oriented northwestward. The water in the submerged valley is generally shallower than 70 m. The valley's head is situated at (31.4°N, 122.7°E).

Southerly and southeasterly winds prevail over the ECS shelf during the summer East Asian monsoon (June, July, and August) [Chu *et al.*, 2005]. The average wind stress is ~0.02 Pa. The monsoon wind creates a distinct upwelling jet that originates from the shelf between the 30 m and 50 m isobaths off the Zhejiang coast and Hangzhou Bay [Liu and Gan, 2014; Zhao, 1982]. The jet flows northward along the west bank of the submerged valley. A prominent upwelling center has frequently been observed over the head of the valley [Lü *et al.*, 2006]. Observations of a horizontally isolated, colder [Lü *et al.*, 2007], and saltier [Wei *et al.*, 2007] water column in the subsurface layer confirm the existence of the upwelling center. The shelf water in the upwelling center is rich in nutrients and has high primary productivity [Wei *et al.*, 2007; Zhao, 1993], which might have led to the severe hypoxia observed near the valley [Li *et al.*, 2011; Wang, 2009].

It has long been recognized that the along and cross-shore variation of shelf topography controls the spatial variation of the upwelling circulation [e.g., Gan and Allen, 2002; Song *et al.*, 2001]. The alongshore current in the upwelling can deviate greatly from geostrophy over variable bottom topography and strengthen upslope cross-isobath transport [Springer *et al.*, 2009]. Besides commonly known Ekman frictional effect, the cross-isobath transport was often found to be induced by the topographically induced along-isobath

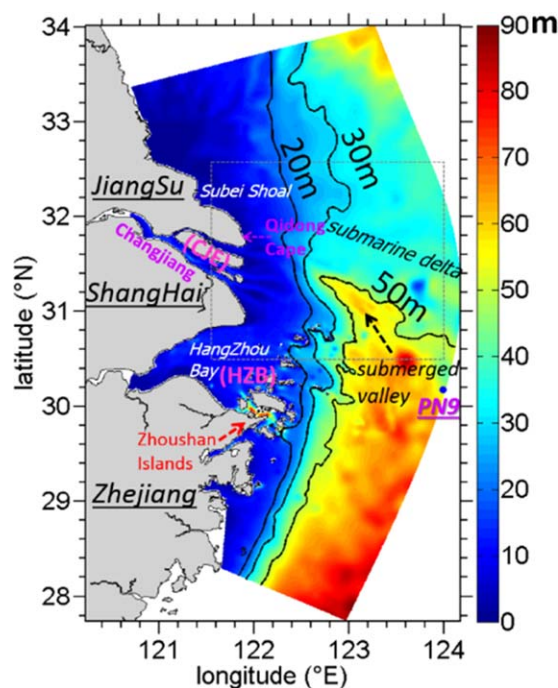


Figure 1. Bathymetry (m) in the ECS and domain of the realistic model. The dashed box indicates the shelf and the location of the submerged valley. The 20, 30, and 50 m isobaths are shown by thick black contours, and PN9 is a field station whose hydrographic property initialized the model.

2005], in laboratory models [Waterhouse *et al.*, 2009], and in field measurements [Allen *et al.*, 2001; Hickey, 1997].

Small-scale topographic features around the canyon can increase the nonlinearity of the shelf circulation [Allen, 2004] and induce an ageostrophic flow that intensifies the upwelling circulation [Allen and Hickey, 2010]. Generally, the upwelling is attributed to the nonlinear dynamics without considering the frictional transport in the bottom boundary layer [Allen and de Madron, 2009]. These nonlinear flow dynamics establishes a high-pressure center over the downstream rim of the submarine canyon [Klinck, 1996]. The high-pressure center causes a negative *PGF* that geostrophically deflects the shelf circulation toward the shore [Flexas *et al.*, 2008]. The circulation amplifies the upslope transport at the head and at the downstream rim of the submarine canyons [Kämpf, 2006]. The strength of the *PGF* is determined by a Rossby number, which is based on the radius of curvature of the isobaths at the upstream rim of the canyon [Allen and Hickey, 2010]. The bottom Ekman process induces the cross-canyon transport. This cross-canyon transport has been ignored in discussions of the upwelling over canyons [Allen and Hickey, 2010; Dawe and Allen, 2010; Kämpf, 2007], but these frictional effects are significant in the depth-integrated barotropic vorticity dynamics of upwelling circulation [Gan *et al.*, 2013; Liu and Gan, 2014]. This is especially true for the highly variable shelf topography of the ECS.

In this study, we combined observational study with numerical modeling and investigated the processes and dynamics of the upwelling around the relatively shallow submerged valley in the ECS.

2. Observational Study

The temperature observations sampled by in situ conductivity-temperature-depth (CTD) measurements in August 2009 during a period of summer upwelling, and the long-term averaged (2002–2012) surface chlorophyll-*a* concentration in summer months (June–August) obtained with the Moderate Resolution Imaging Spectroradiometer (MODIS) are shown in Figure 2.

The temperature distribution displays distinct upwelling that was forced by a strong southeasterly monsoon near the submerged valley. Figures 2a and 2c show that there was relatively cold water at the head of the

pressure gradient force (*PGF*) [Gan and Allen, 2002; Whitney and Allen, 2009]. Gan *et al.* [2013] recently demonstrated the dynamic origin of the *PGF*.

Among the few investigations regarding the mechanics of the upwelling over the submerged valley in the ECS. Lü *et al.* [2006] suggested that the convergence of the tidal residual current in the bottom layer was what led to the upwelling center at the head of the valley. Furthermore, Qiao *et al.* [2006] and Lü *et al.* [2007] pointed out that a baroclinic *PGF* in a tidally generated density front induced the upslope current. However, these studies largely neglected the first-order forcing dynamics that govern the shelf circulation over this unique submerged valley.

Strengthened upwelling over submarine canyons has been studied by many researchers [e.g., Allen and de Madron, 2009; Hickey, 1995; Kämpf, 2006]. Freeland and Denman [1982] observed a persistent pool of dense water near a submarine canyon on the continental shelf off Vancouver Island. Upwelling was also identified in submarine canyons in many numerical simulations [Allen, 2004; Haidvogel,

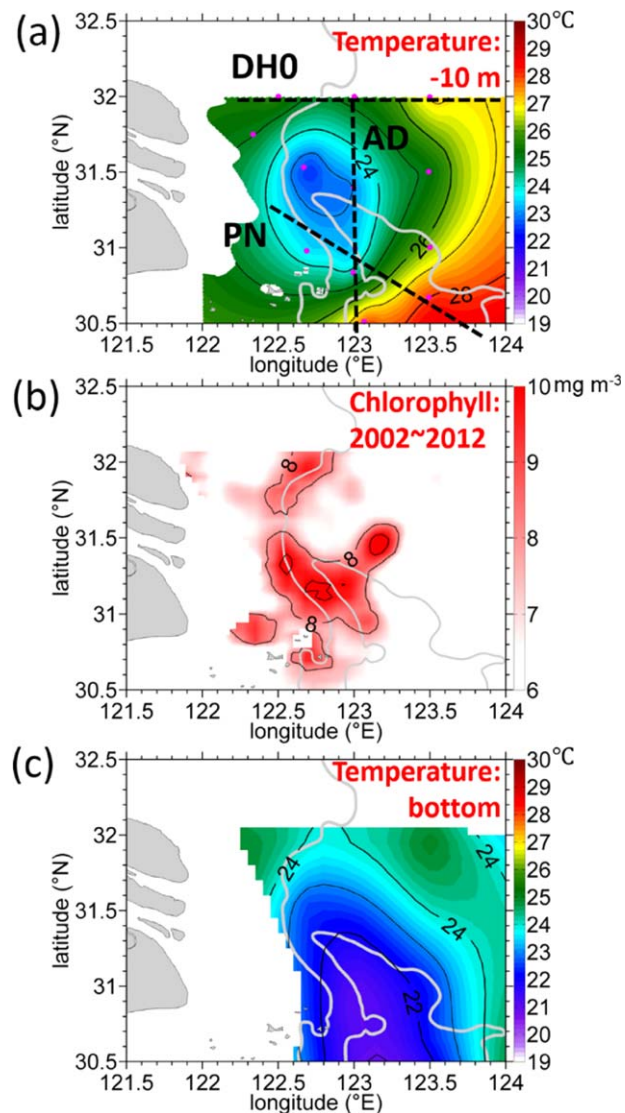


Figure 2. (a) Subsurface (-10 m) temperature ($^{\circ}\text{C}$) sampled from 19 August to 31 August 2009; (b) long-term (2002–2012) averaged remotely sensed surface chlorophyll-*a* concentration (mg m^{-3}) for summer (June–August); and (c) observed bottom temperature ($^{\circ}\text{C}$) distribution. Field stations and three sampling transects are depicted by dashed lines in Figure 2a. The thick gray contours represent the 30 and 50 m isobaths.

These observations confirm the existence of and show the characteristics of the distinct upwelling over the submerged valley. We will conduct a process-oriented numerical modeling study to provide the processes and dynamics underlying the observed upwelling.

3. Modeling Study

3.1. Ocean Model

We conducted a process-oriented simulation to isolate the intrinsic response of the flow to the submerged valley and identify the underlying forcing mechanisms of the observed upwelling.

We used the Regional Ocean Modeling System (ROMS) [Shchepetkin and McWilliams, 2005] to simulate the three-dimensional, time-dependent flow over the study area. We utilized a local closure scheme to parameterize vertical mixing. The closure scheme was based on the level-2.5 turbulent kinetic energy equations of Mellor and Yamada [1982].

valley and along its west bank in the subsurface and bottom layers, respectively. There was a strip of highly concentrated chlorophyll-*a* ($>8 \text{ mg m}^{-3}$) over the valley and intensified along its west bank (Figure 2b). The wind-driven current transported the upwelled deep water near the valley further north between the 30 m and 50 m isobaths. Previous studies have reported similar surface and subsurface features in the region [Lü *et al.*, 2007; Zhao, 1993].

The temperature profiles in Figure 3 show the vertical structure of the upwelling over the valley along survey lines PN, AD, and DH0 (Figure 2a). The upwardly tilting isotherms along PN indicate that relatively strong upwelling occurred over the west bank (Figure 3a). The northward and upward isotherms along AD (Figure 3b) indicate that the upwelled cold water advected northward along the isobaths (also see Figure 2c). The upwelling center at the head of the submerged valley formed a cold-water filament, in the bottom layer, between 122.5°E and 123.3°E across line DH0 (Figure 3c).

The temperature profiles in Figure 4 also reveal spatially variable upwelling over the submerged valley along the 30 and 50 m isobaths that border the valley. Along the 30 m isobath, isotherms (e.g., 24°C) near the bottom gradually rose from the south toward the head and then descended north of the head. Two cold centers were found along the west bank and around the head of the valley, which is consistent with Figures 2 and 3. Similar upwelling characteristics are seen in the spatial pattern along the 50 m isobath (Figure 4b).

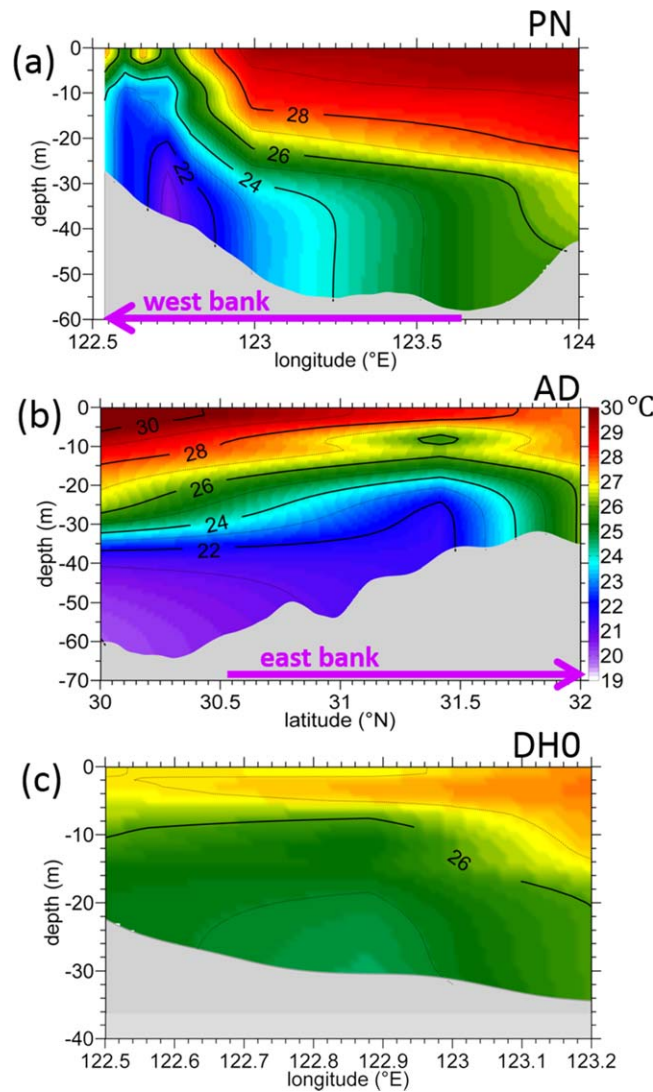


Figure 3. Observed vertical temperature ($^{\circ}\text{C}$) profiles along the survey lines (a) PN, (b) AD, and (c) DH0 near the submerged valley.

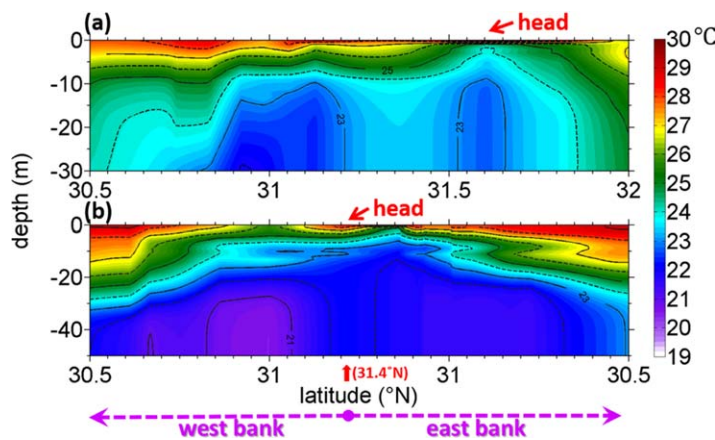


Figure 4. Observed temperature ($^{\circ}\text{C}$) profiles along (a) the 30 m and (b) the 50 m isobaths bordering the submerged valley. See Figure 2a for isobath positions.

The model domain extended from 27.75°N to 34°N and from 120.7°E to 124.2°E (Figure 1). The horizontal mesh (x, y) was a curvilinear grid with a (358,666) dimensional array. There was a higher resolution horizontal grid ($\Delta x, \Delta y \approx 0.2\text{km}$) in the coastal regions west of the 30 m isobath. The grid size gradually increased to $\sim 1.5\text{ km}$ in the open ocean [Liu and Gan, 2014]. We digitized a realistic coastline and bottom topography from navigation maps published by the Maritime Safety Administration (China). We smoothed the topography slightly to reduce truncation errors. We also adapted the stretched, generalized, terrain-following s coordinate system [Song and Haidvogel, 1994] to discretize the water column with a minimum water depth of 1 m. We used controlling parameters of $\theta_s = 2.5$ and $\theta_b = 0.8$. The controlling parameters represented a higher vertical resolution ($< 0.3\text{ m}$) in both the surface and bottom boundary layers, respectively, while avoiding the artificial diffusion that a larger vertical grid spacing in the central part of the water column could cause [Gan et al., 2009].

Process-oriented simulation was conducted in this study to isolate the topographical effect and identify the underlying forcing mechanisms of upwelling over the submerged valley. Thus, we adapted horizontally homogeneous initial conditions and used field measurements from station PN9 for the initial temperature and salinity. To retrieve the real dynamics, it was advantageous to initialize the model with zero velocities and surface elevation and to force the model with a spatially uniform southeasterly wind

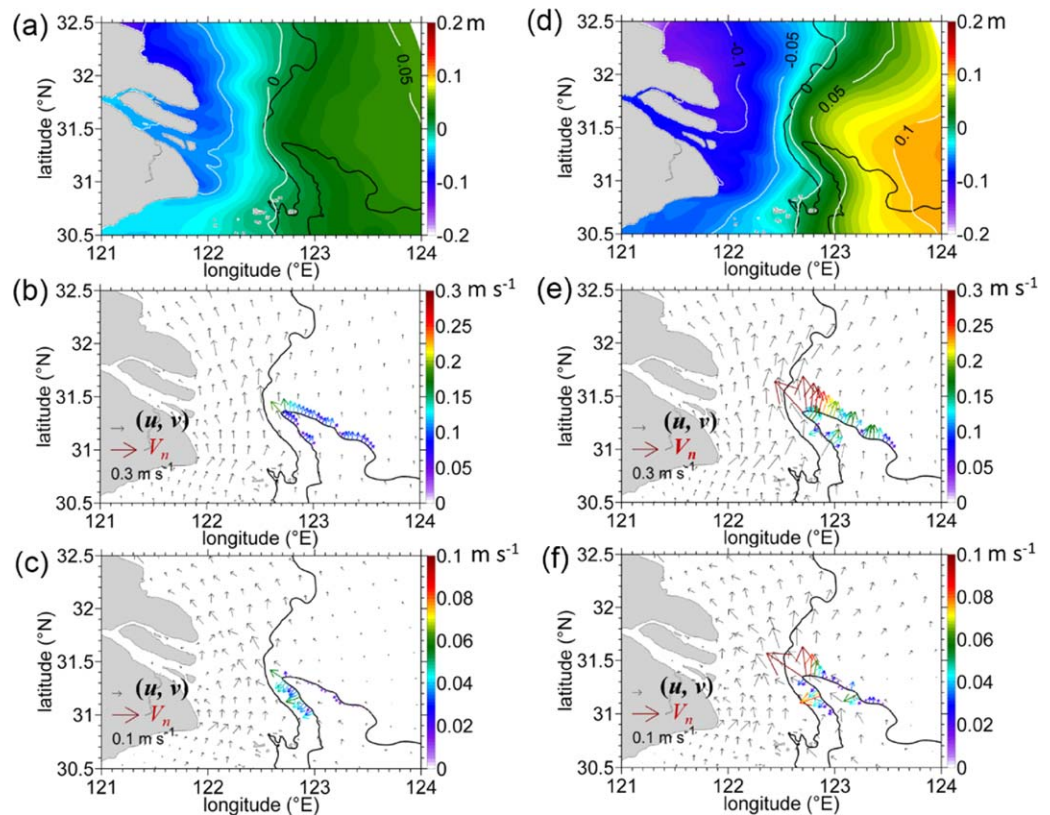


Figure 5. (a, d) Daily averaged simulated surface elevation (m), (b, e) surface velocity (m s^{-1}), and (c, f) bottom velocity vectors (m s^{-1}) on (left) day 5 and (right) day 30. Components of the surface and bottom velocities normal to the 50 m isobath on (b, c) day 5 and (e, f) day 30 are indicated by the colored vectors (V_n). The bold black lines represent the 30 and 50 m isobaths. Different scales for the unit vectors in Figures 5b and 5e and Figures 5c and 5f were used.

stress for 30 days. We set the meridional and zonal components of wind stress equal to 0.0181 and -0.0125 Pa, respectively. These wind stress values were representative of the upwelling favorable summer monsoon over the ECS [Liu and Gan, 2014].

The model domain included three open boundaries (OBs). We used an “active” open boundary condition (OBC) suitable for coastal simulations with limited area [Gan and Allen, 2005; Gan et al., 2005] on the northern and southern OBs. We adapted an oblique horizontal radiation OBC [Marchesiello et al., 2001] at the eastern boundary for barotropic (\bar{u}, \bar{v}) and baroclinic velocities (u, v), temperature (T), and salinity (S). We applied a no-gradient OBC to the surface elevation (η). Because we were interested in the intrinsic dynamic response of a wind-driven coastal current to the submerged valley, we ignored tidal forcing and remote current intrusions in the ECS.

3.2. Circulation in the Horizontal Plane

We averaged the simulated surface elevation (η) and velocity (u, v) vectors for the surface and bottom layers on days 5 and 30. The averaged values show that there was a spatiotemporal variation in the upwelling circulation over the submerged valley in the horizontal plane (Figure 5). The surface and bottom velocity vectors normal to the 50 m isobath (V_n) are also shown in Figure 5. We call V_n the “cross-bank” velocity, which indicated the flow entering ($V_n < 0$, downslope) or leaving ($V_n > 0$, upslope) the valley across the banks. The velocity along the isobaths (V_s , positive northward) is the “along-bank” velocity.

The isolines of η (Figures 5a and 5d) oriented in the alongshore direction in response to the southeasterly wind stress. Their cross-shore gradients formed geostrophic currents that flowed along the bank over the shelf (Figures 5b and 5e). Both the gradients and the currents strengthened and shifted eastward from day 5 to day 30. The coastal current evolved into a prominent jet on day 30. The jet’s core was over the relatively steep shelf, in the strip bounded by the 30 and 50 m isobaths, west of the west bank (Figure 5e).

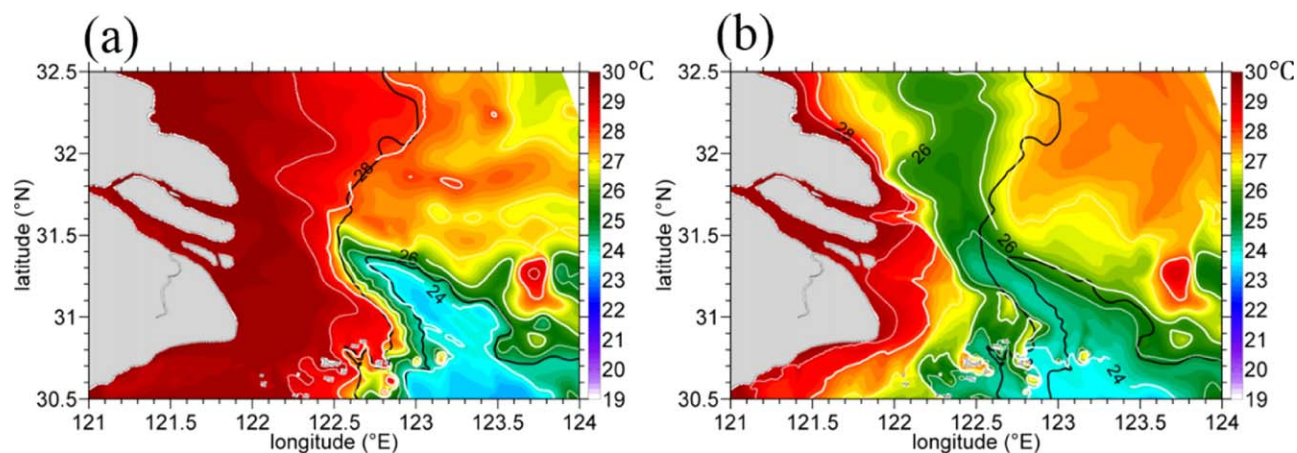


Figure 6. Simulated bottom temperature ($^{\circ}\text{C}$) distributions averaged on (a) day 5 and (b) day 30. The thick black lines represent the 30 m and 50 m isobaths.

The cross-bank current (V_n) was the major contributor to the upwelling over the valley. This current exhibited a remarkable spatial variation. Because of the southeasterly wind forcing, there was northeastward surface transport over the valley (Figures 5b and 5e). At the bottom, frictional effects formed an upslope V_n along the 50 m isobath (Figures 5c and 5f). The positive V_n intensified over the west bank. It peaked at the head of the valley due to the presence of a southward PGF (Figures 5a and 5d). Allen [2000] and Kämpf [2006] also found that high pressure over a topographic valley enlarged the zonal elevation gradient at the head and created a PGF that enhanced the cross-bank transport near the head.

The intense cross-bank transport along the west bank and at the head of the valley at the bottom (Figures 5c and 5f) advected cold deep water upslope. The cold water, subsequently, extended northward over the submarine delta on day 30 (Figure 6). The cold water formed the distinct cold center at the head seen in Figures 2 and 3. The upslope motion of cold deep water (e.g., see the 24°C isotherm) was much weaker along the east bank, as seen in the observations. The advance of waters in the valley was consistent with the velocity field.

3.3. Circulation in the Vertical Plane

Figure 7 shows simulated velocity profiles along the 50 m isobath of the three-dimensional upwelling circulation surrounding the submerged valley. We rotated the horizontal velocity (u, v) to the cross-bank (V_n) and along-bank (V_s) velocities and show the results for day 30.

Strong V_s flowed northward (resp. northwestward) along the west (resp. east) bank and occupied the entire water column with a strengthened (resp. weakened) magnitude around the valley's head (resp. near the bottom) (Figure 7a). Surface water generally deflected downslope ($V_n < 0$) and a notable upslope compensating flow ($V_n > 0$) formed in the lower layer at the west bank. The upslope current ($V_n > 0$) responded to the considerable negative along-bank PGF and occupied almost the entire water column at the east bank next to the head (Figure 5d). The concurrent very strong upward ($w > 0$) motions near the head of the valley and along the west bank indicate locally intensified upwelling. Meanwhile, a strong upslope current ($V_n > 0$) formed in the upper layer along the east bank. The upslope current was suppressed by the downslope ($V_n < 0, w < 0$) current flowing in the bottom layer. We saw similar features in the field measurements (Figure 4b).

Figure 8 shows the temperature variation over the valley. The variation is similar to the observed ones in Figure 3. It was also consistent with the velocity along the 50 m isobath in Figure 7. Deep shelf water, originally from the shelf farther offshore, moved upslope along transect PN to the subsurface layer over the west bank. The coastal current carried these upwelled deep waters northward to form an isolated cold-water filament in the bottom layer at line DH0. The filament also eventually led to the surface cold water over the shallower Subei Shoal. However, the bottom isotherms (e.g., 24°C) over the submarine valley

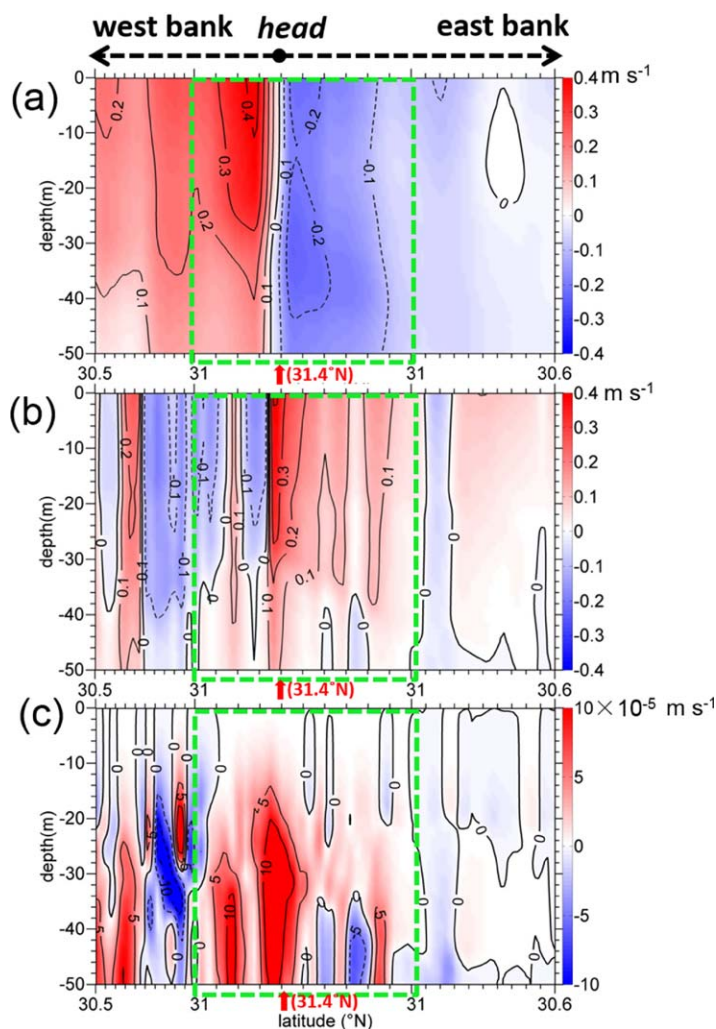


Figure 7. Simulated (a) along-bank (V_s , m s^{-1}), (b) cross-bank (V_n , m s^{-1}), and (c) vertical (w , m s^{-1}) velocities along the 50 m isobath. The model results are averaged on day 30. The location of the 50 m isobath is presented in Figure 2a. Positive values denote the (a) northward (resp. southeastward) and (b) westward (resp. northeastward) velocities on the west (resp. east) bank of the submerged valley, and (c) upward velocity. The 50 m isobath, adopted in the discussion of V_n in Figure 5, is enclosed by the green box.

depth in the submerged valley was 60 m, and the depth of the surrounding shelf was 30 m. The west and east banks deepened toward the valley with a slope of $\sim 1.0 \times 10^{-3}$ which is similar to the actual ECS bathymetry.

To utilize a well-defined periodic OBC in this idealized simulation, we defined a mirrored, but reversed, symmetric bathymetry in a northern region, over the shelf, at $2500 \text{ km} < y < 2580 \text{ km}$, $\sim 800 \text{ km}$ away from the valley. We imposed the oblique horizontal radiation OBC [Marchesiello *et al.*, 2001] on the eastern boundary for the barotropic (\bar{u}, \bar{v}) and baroclinic velocities (u, v), temperature (T), and salinity (S). We applied a no-gradient OBC to the surface elevation (η).

We forced the model with a spatially uniform southeasterly wind stress for 20 days, which was when the model reached a quasi-steady state. The magnitude of the wind stress was $\sim 0.02 \text{ Pa}$ with the meridional and zonal components equaling 0.0181 and -0.0125 Pa , respectively. The other dynamic configuration and numerical implementations were similar to the simulation with realistic topography described in section 3. To highlight the topographic effect of the variable upwelling over the submerged valley, we conducted a barotropic simulation by adapting a spatially homogeneous density field as the initial condition.

retreated downslope along line AD. This signified an absence of strong upwelling in the bottom layers at the east bank. These simulated features are very similar to our observations (Figure 3).

The simulated temperature profile along the 50 m isobath over the valley (Figure 8d) is similar to our observations too (Figure 4). Intense upwelling merely occurred over the west bank, where there was much colder deep shelf water than over the east bank. Upwelling peaked at the head, where the isotherms rose considerably.

4. Dynamic Analyses

Because of the extremely complex bathymetry in the north-west ECS, we adapted a conceptual simulation with simplified topography of the valley to study the forcing mechanisms. The domain of the idealized model extended 250 and 3200 km in the zonal and meridional directions, respectively (Figure 9). The horizontal resolution was 1.5 km. A submerged valley, broadening toward the southeast, was positioned over the midshelf between $1600 \text{ km} < y < 1680 \text{ km}$. The water

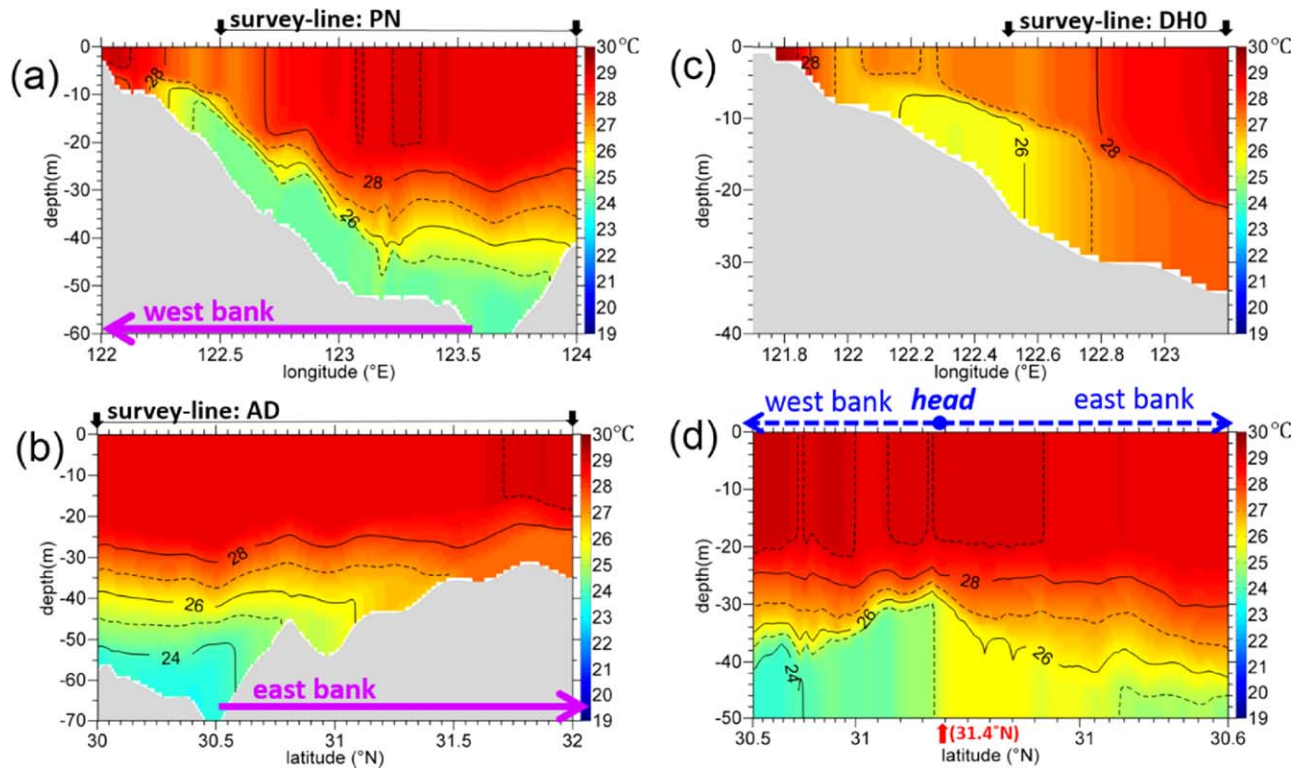


Figure 8. Simulated temperature ($^{\circ}\text{C}$) profiles along the survey lines of (a) PN, (b) AD, and (c) DH0 over the submerged valley. (d) The profile along the 50 m isobath. The area covered by the survey lines PN, DH0, and AD are indicated at the top of Figures 8a–8c. The temperature is averaged on day 30. The locations of the survey transects are presented in Figure 2a.

4.1. Flow Field

Figure 9 shows the general characteristics of the variable upwelling over the submerged valley under the quasi-steady state on day 20. The figure contains the surface elevation and the surface and bottom velocity vectors. In Figure 9a, it can be seen that the eastward pressure gradient caused the associated coastal current to flow northward in a strip between the 30 m and 50 m isobaths along the west bank. This is where deep shelf water intruded upslope in the bottom layer (Figure 9b). This result is consistent with our results from the realistic model shown in Figure 5. Our work revealed that a high-pressure center, shown by the isolines with $\eta > 0$, occupied the area north of the east bank, where the coastal current flowed northward. At the head of the submerged valley, the coastal current intensified (Figure 9a). The high-pressure center caused the current's mainstream to circulate anticyclonically.

Figure 10 shows the along-bank (V_s), cross-bank (V_n), and vertical (w) velocities (m s^{-1}). As in the process-oriented study with realistic topography, we rotated the horizontal velocities to the along (V_s) and cross-bank (V_n) directions over the 50 m isobath (Figure 10). Along the west bank ($1450 \text{ km} < y < 1680 \text{ km}$, Figure 10a), there was a strong northward coastal current ($V_s > 0$) and deep water intruded upslope below the surface ($V_n > 0$, $w > 0$). The velocities with $V_s > 0$, $V_n > 0$, and $w > 0$ intensified northward and reached their maxima at the head of the valley. The coastal current along the east bank flowed northwestward ($V_s < 0$) and were shaped geostrophically by the high-pressure center. Although the positive cross-bank current was still flowing in the upper layer along the east bank, the local upwelling, as indicated by the cross-bank velocities near the bottom layer, diminished away from the head. The circulation over the idealized topography was very similar to that over the realistic topography (Figure 7).

Figure 11 illustrates the along-bank variations in η , relative vorticity (ξ) decomposed into shear (ξ_s) and curvature (ξ_c) vorticity, and the depth-averaged along-bank (\bar{V}_s) and cross-bank (\bar{V}_n) velocities along the 50 m isobath. η , \bar{V}_s , \bar{V}_n , and negative ξ_s amplified along the west bank and peaked at the head ($y = 1680 \text{ km}$). The high-pressure center had intense negative ξ_c in the anticyclonic circulation due to a vertically squeezed vortex tube or nonlinear advection of vorticity (see subsection 4.2). The high-pressure center was located at

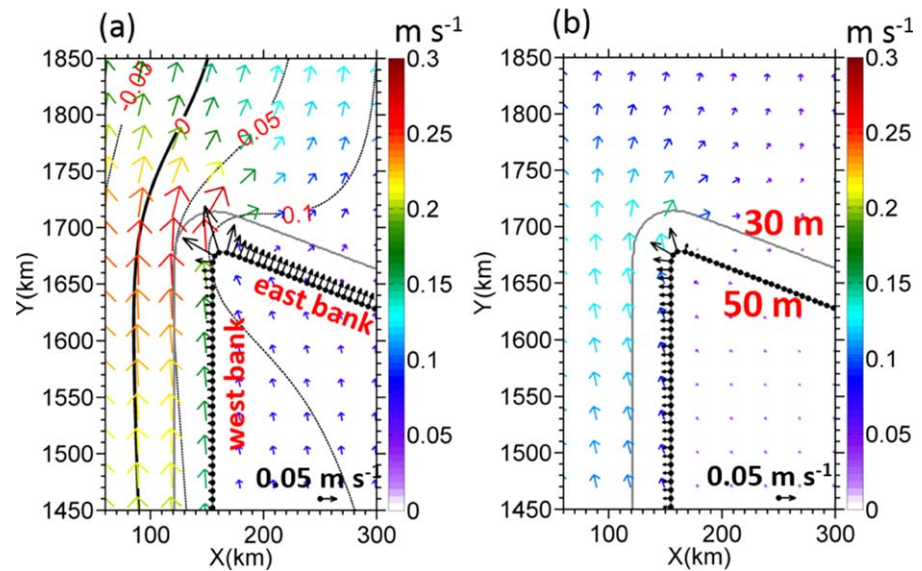


Figure 9. Simulated (a) surface velocity (m s^{-1}), elevation (m, contour lines), and (b) bottom velocity (m s^{-1}) vectors on day 20. The gray lines outline the submerged valley and depict the 30 m and 50 m isobaths. The components of the surface and bottom velocities normal to the 50 m isobath are indicated by the black vectors in Figures 9a and 9b.

the northeast of the head (Figure 11a). \bar{V}_n and the associated ζ_s decreased quickly away from the head along the east bank. This is the coastal current deflected northwestward ($\bar{V}_s < 0$) and flowed toward the head.

4.2. The Momentum and Vorticity Balances

We conducted analyses of the momentum and vorticity balances based on the idealized simulation to determine the dynamics of the upwelling over the submerged valley.

4.2.1. The Cross-Bank and Along-Bank Balances

In the absence of stratification and wind stress curl, the depth-averaged momentum (equation (1)) and vorticity (equation (2)) equations, in the Cartesian coordinate system, are written as [Liu and Gan, 2014]

$$ACCEL = COR + HADV + PGF + SSTR + BSTR + HVISC, \quad (1)$$

$$\nabla \times ACCEL = \nabla \times HADV + \nabla \times COR + \nabla \times BSTR + \nabla \times HVISC, \quad (2)$$

where ∇ is the Hamiltonian operator.

The terms in (1) are acceleration ($ACCEL$), Coriolis force (COR), horizontal nonlinear advection ($HADV$), pressure gradient force (PGF), wind stress ($SSTR$), frictional bottom stress ($BSTR$), and the horizontal viscous term ($HVISC$). The ageostrophic pressure gradient force ($AGE = PGF + COR$) is adapted to consider the combined effects of COR and PGF [Gan et al., 2009]. The terms in (2) are the tendency of the ζ ($\nabla \times ACCEL$), advection of ζ ($\nabla \times HADV$), vertical stretching of the vortex tube ($\nabla \times COR$), bottom stress curl ($\nabla \times BSTR$), and lateral frictional effects ($\nabla \times HVISC$).

The terms in (1) and (2) along the 50 m isobath, on day 20, are shown in Figure 12. To better understand the intrinsic dynamics of the variable upwelling around the valley, we rotated the terms in (1) to the along-bank and cross-bank directions, denoted by the subscripts s and n , in Figures 12a and 12b, respectively.

The wind-induced Ekman transport caused a positive cross-bank PGF_n . The result was a geostrophic northward coastal current along the west bank (Figure 12a). Along the east bank, a negative PGF_n generated a northwestward current. The along-bank momentum balance (Figure 12b) clearly shows a distinct southward PGF_s that geostrophically enlarged the positive \bar{V}_n (Figure 11b) and generated the extensive upslope advection of deep shelf water along the west bank and at the head of the valley. The bottom Ekman dynamic contribution was much weaker.

As the coastal current flowed northward across the 30 m isobath at the head of the valley and into the shallower submarine delta (Figure 9a), the vortex tube was vertically squeezed ($\nabla \times COR < 0$,

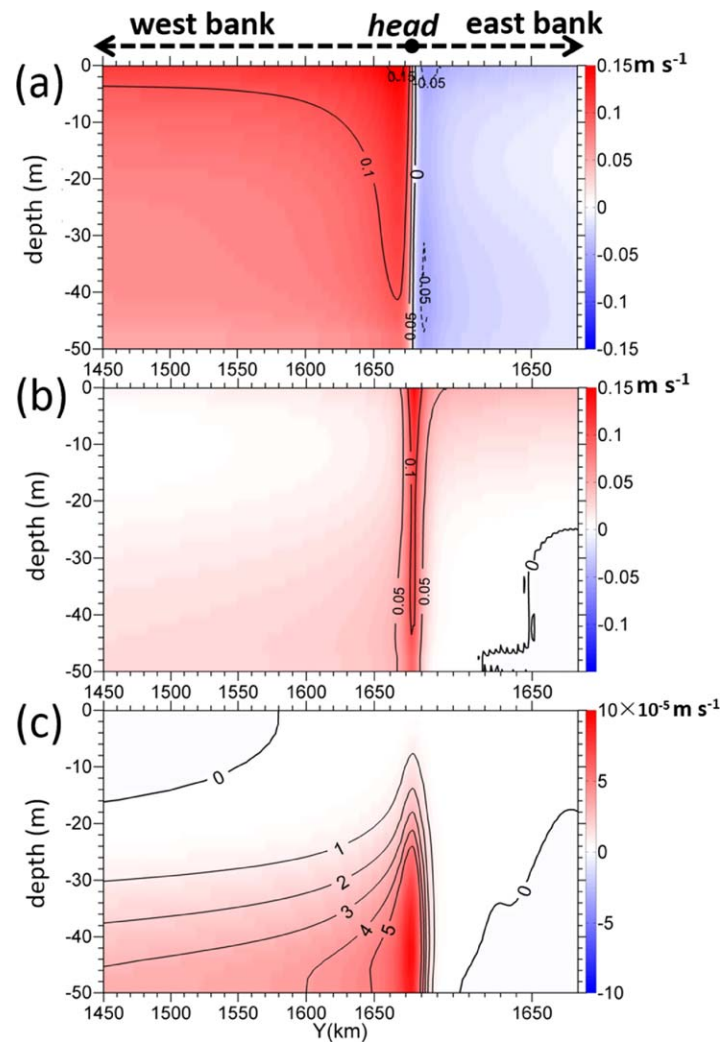


Figure 10. Vertical transects of simulated (a) along-bank (V_s), (b) cross-bank (V_n), and (c) vertical velocities (m s^{-1}) along the 50 m isobath on day 20. Positive values of V_s and V_n denote the (a) northward (resp. southeastward) and (b) westward (resp. northeastward) velocities on the west (resp. east) bank of the submerged valley, and the (c) upward velocity. The orientation of the 50 m isobath is illustrated in Figure 9b, and $Y = 1650$ km is labeled for the west and east banks, once for each bank.

intensified upslope intrusion of deep water along the west bank and around the head. The northward elevated η (Figure 11a), or the negative along-bank PGF_s (Figure 12b), weakened the intrusion along the east bank but enhanced it along the west bank. This was apparent in both the observations (section 2) and simulations (section 4).

The bottom stress curl and nonlinear vorticity advection both contributed to PGF_s . Gan *et al.* [2013] termed the PGF_s at the bottom PYB and expressed it as $\frac{-1}{\rho_0} p_{y^*}^b$, based on the depth-integrated vorticity equation

$$\frac{-1}{\rho_0} p_{y^*}^b = \overbrace{\frac{1}{D_{x^*}} \nabla \times \left(\frac{\tau_b}{\rho_0} - \frac{\tau_s}{\rho_0} \right)}^{BSC} + \overbrace{\frac{1}{D_{x^*}} J(\psi, \xi)}^{RVA} + \overbrace{\left(\frac{\|\vec{v}\|^2}{2} \right)_{y^*}}^{GMF}, \quad (3)$$

where the subscripts x^* and y^* denote partial differentiation in the cross-bank and along-bank directions, respectively. $\frac{-1}{\rho_0} p_{y^*}^b$ refers to the along-bank pressure gradient force at the bottom and in this barotropic case, it equals the along-bank PGF_s . D_{x^*} is the cross-bank sloping parameter along the 50 m

Figure 12c) and relative vorticity (ξ) was reduced (Figure 11a). The current at the head rotated anticyclonically because of the negative advection of relative vorticity. This negative advection is illustrated by the dominant balance between the nonlinear advection term ($\nabla \times HADV$) and the stretching term ($\nabla \times COR$) around the head in Figure 12c. In contrast, the stretching term ($\nabla \times COR$) was mainly ($\sim 80\%$) balanced by the bottom stress curl ($\nabla \times BSTR$) upstream (e.g., $y < 1500$ km) along the west bank (Figure 12c). This bottom stress curl ($\nabla \times BSTR$) peaked at the head and compensated a portion ($\sim 33.1\%$) of the stretching term ($\nabla \times COR$). In fact, the combined effect of nonlinear advection and bottom stress curl contributed to the formation of the negative along-bank PGF_s (see below) and enhanced the upslope motion over the valley.

4.2.2. Origin of PGF_s

In the previous discussion, we identified a negative along-bank PGF_s that generated extensive upwelling along the west bank and that created the

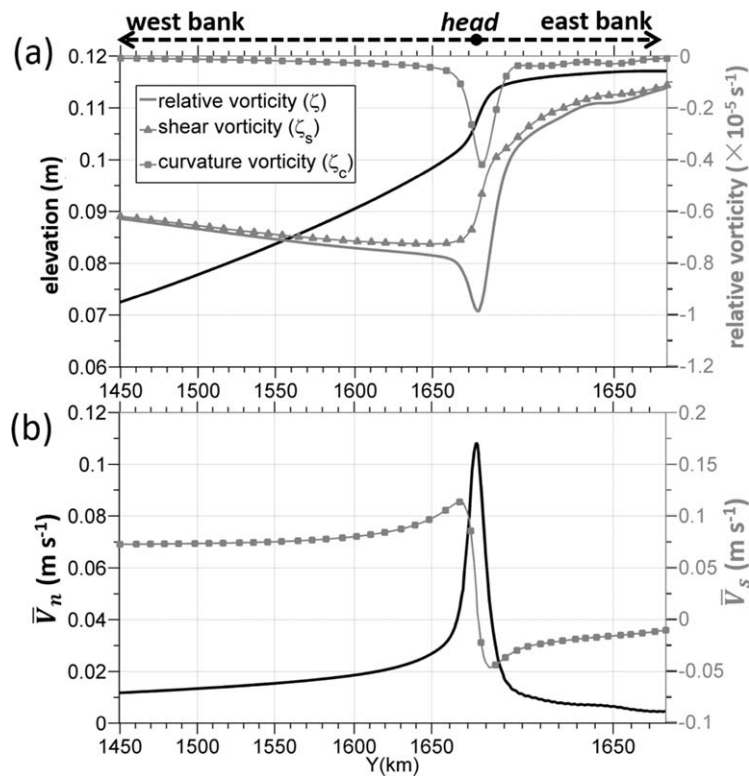


Figure 11. (a) Surface elevation (m, solid black line), shear and curvature vorticity (s^{-1} , gray lines); (b) simulated depth-averaged cross-bank (\bar{V}_n) and along-bank (\bar{V}_s) velocities ($m s^{-1}$) along the 50 m isobath. The model results are averaged on day 20. Positive values of \bar{V}_s and \bar{V}_n in Figure 11b denote the northward (resp. southeastward) and westward (resp. northeastward) velocities along the west (resp. east) bank. The orientation of the 50 m isobath is illustrated in Figure 9b, and $Y = 1650$ km is labeled for the west and east banks, once for each bank.

isobath. J is the Jacobian determinate, and ψ is the transport stream function. \vec{v} is the vector form of the depth-averaged velocity in the zonal (\bar{u}) and meridional (\bar{v}) components.

The terms on the right-hand side of (3) are the net stress curl of the water column, which represents the bottom stress curl (BSC) when the wind stress curl is absent; relative vorticity advection (RVA); and the gradient of momentum flux (GMF). The terms in (3) along the 50 m isobath on day 20 are displayed in Figure 13a. In addition, under the approximation of the quadratic drag law, BSC can be expressed as [Liu and Gan, 2014]

$$\overbrace{\frac{1}{D_{x^*}} \nabla \times \frac{\tau_b}{\rho_0}}^{BSC} = \overbrace{\frac{C_d}{D_{x^*}} \|V_b\| \zeta_{bc}}^{BSC_c} + \overbrace{\frac{2C_d}{D_{x^*}} \|V_b\| \zeta_{bs}}^{BSC_s}, \quad (4)$$

where $C_d = 3 \times 10^{-3}$ is the bottom drag coefficient and V_b is the magnitude of the bottom velocity. ζ_{bs} is the bottom shear vorticity and ζ_{bc} represents the curvature vorticity at the bottom. The bottom relative vorticity (ζ_b) can be obtained from the sum of ζ_{bc} and ζ_{bs} . BSC_c and BSC_s represent the contributions of ζ_{bc} and ζ_{bs} to the bottom stress curl (BSC), respectively. BSC_c and BSC_s along the 50 m isobath are shown in Figure 13b.

Figure 13a shows the contribution of the terms in equation (3) to the negative PGF_s . PGF_s gradually increased toward the head of the valley. The negative BSC, or the negative bottom vorticity, ζ_b (equation (4)), was the major contributor to PGF_s along the west bank and far from the head. The shear of the coastal current along the west bank contributed to negative BSC, and ζ_{bs} is the main source of ζ_b . This ζ_{bs} generated extensive BSC, and, then, southward PYB (Figure 13a) that geostrophically forced the upslope cross-bank transport along the west bank.

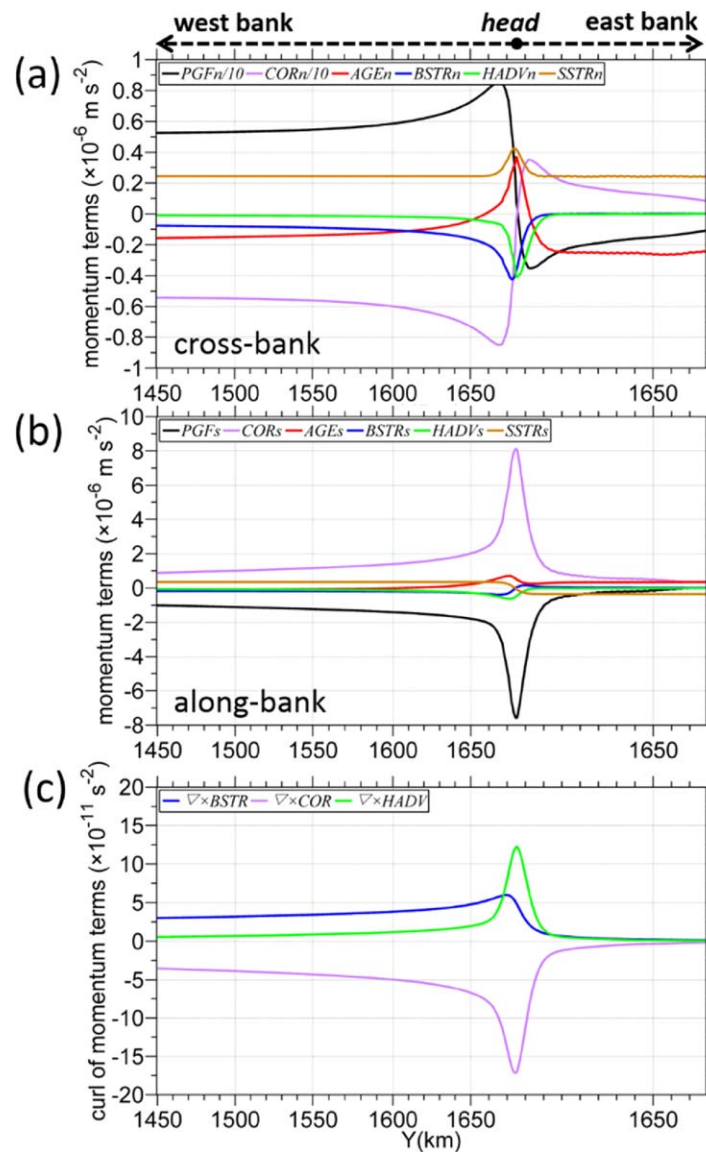


Figure 12. Terms (m s^{-2}) of the depth-averaged momentum equations in (a) cross-bank, and (b) along-bank directions, and (c) terms (s^{-2}) in the depth-averaged relative vorticity equation along the 50 m isobath. Positive values represent the momentum terms in (a) the westward (resp. northeastward) direction and (b) the northward (resp. southeastward) direction over the west (resp. east) bank. All the variables are averaged on day 20, and the PGF_n and COR_n in Figure 12a are scaled by 10. The orientation of the 50 m isobath is illustrated in Figure 9b, and $Y = 1650$ km is labeled for the west and east banks, once for each bank.

locally maximized RVA contribution to PGF_s . Extensive upwelling vanished at the east bank, because of the absence of the strong RVA and BSC .

Nevertheless, the nonlinear advection effect amplified substantially as the coastal current that flowed over the valley strengthened. The underlying upwelling dynamics associated with the nonlinearity or with the vertically squeezed vortex tube over the valley were similar to those found in submarine canyons [Allen, 2000; Klinck, 1996]. The canyon studies, however, focused on the effect of nonlinear ageostrophy on the upwelling while ignoring the role of bottom stress. But in fact, both nonlinearity as RVA and bottom frictional effects as BSC contribute to the formation of PGF_s for the upslope transport, according to equation (3). Next, we discuss the relative importance of both nonlinearity and bottom stress curl to the upwelling over the valley.

The condition at the head of the valley was quite different. Although the magnitude of BSC was still quite large, RVA became the major source of the negative PGF_s . Because of the vertical squeezing of the vortex tube and the intensified coastal current, both the curvature vorticity (ξ_{bc}) and shear vorticity (ξ_{bs}) ($y = 1680$ km) peaked locally and generated the considerably negative RVA at the head. As a result, PGF_s peaked at the head to maximize the upwelling by geostrophically moving the deep water up the slope. Both RVA and BSC quickly weakened away from the head along the east bank, as did vorticity (Figure 11a) and the upslope motion (Figure 11b).

5. Nonlinearity Versus Frictional Effects

We have shown that the formation of the negative along-bank PGF_s amplified the cross-bank transport along the west bank. The negative shear vorticity on the seaside of the along-bank jet current caused a negative BSC_s that contributed to the PGF_s . We also found that the nonlinear vorticity advection of the coastal current dominated the formation of the strongest upslope current near the head where we observed the

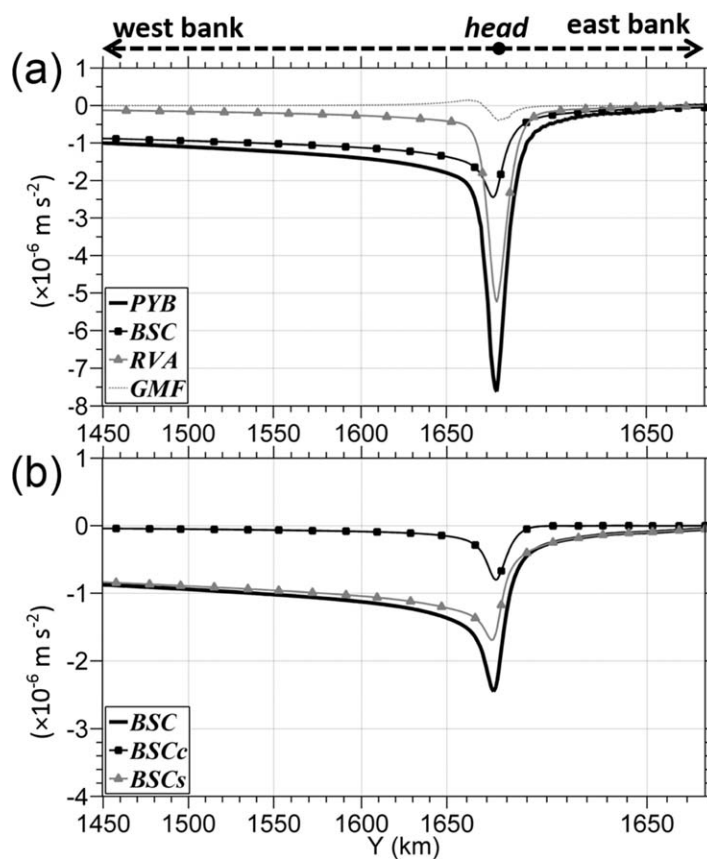


Figure 13. (a) Terms (m s^{-2}) in the depth-integrated relative vorticity equation (equation (3)) along the 50 m isobath on day 20. (b) Contributions of bottom shear and curvature vorticity to the total bottom stress curl (equation (3)) are represented by BSC_s and BSC_c , respectively. A positive PYB value represents the northward (resp. southeastward) direction along the west (resp. east) bank. The orientation of the 50 m isobath is illustrated in Figure 9b, and $Y = 1650$ km is labeled for the west and east banks, once for each bank.

converged. The characteristic of maximum coastal current at the head agreed with our previous result for the standard case in Figure 9. However, the positive along-bank η gradient formed a stronger cross-bank transport over the west bank and at the head than in the standard case in Figure 9a. Unlike in the standard case (Figure 9b), the extensive upslope transport of deep shelf water occurred in the bottom layer along the east bank near the head as well (Figure 14b). The magnitude of this upslope current was comparable to that at the west bank. A notable positive along-bank gradient of η (Figure 14a) generated a remarkable negative PGF_s along the east bank and induced the upslope current. This sensitivity experiment showed the extension of the upwelling circulation around the head of the east bank, when a stronger coastal current was established in the ECS.

Although the structures of the cross-bank (\bar{V}_n) and along-bank (\bar{V}_s) velocities along the 50 m isobath (Figure 15) remained similar to the standard case in Figure 11, their magnitudes increased greatly. A significant increase in \bar{V}_n occurred along the east bank around the head, accompanied by a concurrent increase in vorticity. The enhancement in the vorticity along the east bank was mainly attributed to the increase in curvature vorticity due, in turn, to the intensified current over the curving isobaths around the head.

As a result, the dynamic formation of PGF_s for the upwelling along the west bank and at the head proved to be robust. The major contributor to the intensified negative along-bank PGF_s was the locally increased BSC over the west bank, where there was a slightly concurrent increased RVA (Figure 16a). The RVA/PGF_s ratio represents the contribution of the nonlinear effect to the negative along-bank PGF_s . The ratio increased slightly to ~ 7.5 from $\sim 1.5\%$ in the standard case along the west bank (Figure 13a).

We conducted a sensitivity experiment over the idealized valley by increasing the wind stress from ~ 0.02 Pa in the standard case to ~ 0.1 Pa. The meridional and zonal components were set to 0.0905 and -0.0625 Pa, respectively. This increased wind stress significantly strengthened the current over the shelf and represented the dynamic scenario of the current being intensified by, for example, an augmented intrusion of the Kuroshio Current, spring tidal current and episodic strong wind forcing [Yang *et al.*, 2012].

Figure 14 shows the horizontal distribution of η , and the surface and bottom velocity vectors on day 20 from this sensitivity experiment. The coastal current in the entire water column over the shelf was stronger than that forced by the standard wind stress in Figure 9. This was because of the amplified cross-bank PGF_n (i.e., gradient of η) in response to the wind stress forcing. This coastal current peaked at the head where the isolines of η

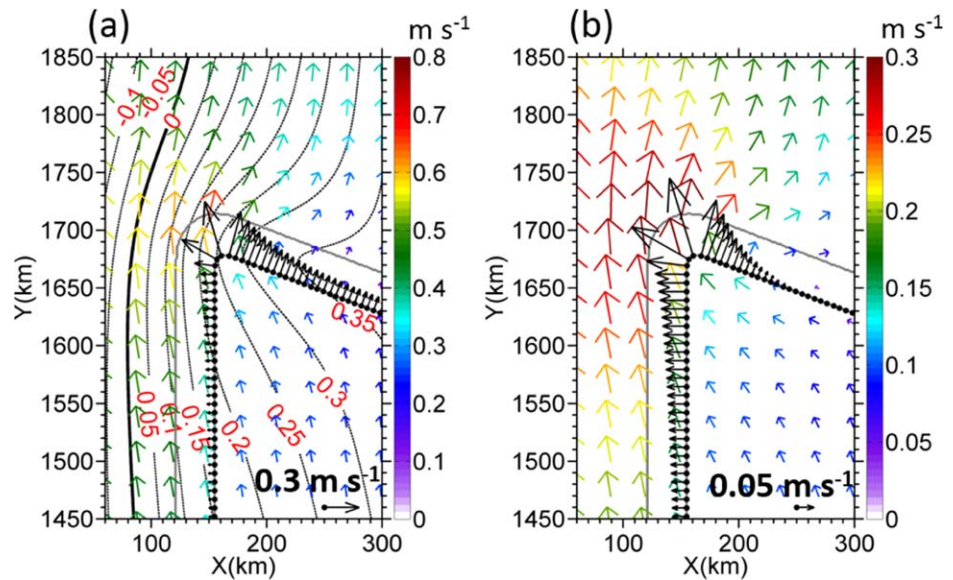


Figure 14. (a) Surface velocity vectors (m s^{-1}), elevation (m, contour lines), and (b) bottom velocity (m s^{-1}) vectors in the case of increased wind stress. The velocity and elevation fields are averaged on day 20. The gray/black lines are the 30 and 50 m isobaths. The components of the surface and bottom velocities normal to the 50 m isobath are indicated by the black vectors in Figures 14a and 14b. Note that the color scale and velocity vector scale in Figure 14a are larger than those in Figure 14b.

A stronger negative relative vorticity (ζ) existed on the seaside of the accelerated coastal current (Figures 15 and 16c). This vorticity was the main source of the intense PGF_s . At the same time, the nonlinearity of the coastal current contributed more to the locally maximized PGF_s at the head of the valley. In response to the augmented negative relative vorticity (ζ , Figure 16c), the RVA/PGF_s ratio near the head increased to

$\sim 73.4\%$ (Figure 15a) from $\sim 65.7\%$ in the standard case (Figure 13a).

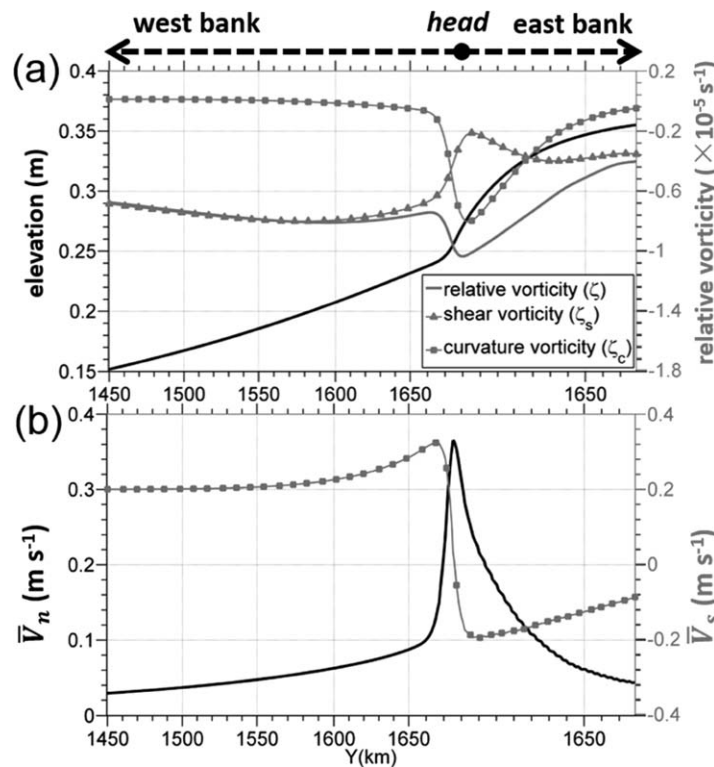


Figure 15. Same as Figure 11 but for the case forced with wind stress magnitude of 0.1 Pa.

In contrast to the standard experiment (Figure 13a), an intensified along-bank PGF_s was established around the head at the east bank in the case of a strengthened coastal current (Figure 16a). It revealed that the amplified RVA was the main contributor to PGF_s , and the contribution from BSC to PGF_s was relatively weak. The contributions of both BSC_s and BSC_c (not shown) to BSC at the east bank also increased compared to the standard case. This was due to the presence of a strong negative curvature vorticity over the curving head (Figures 15 and 16c). These results suggest that the nonlinear effect played a larger role in the cross-bank transport as the coastal current grew stronger. RVA alone may be able to drive the cross-bank

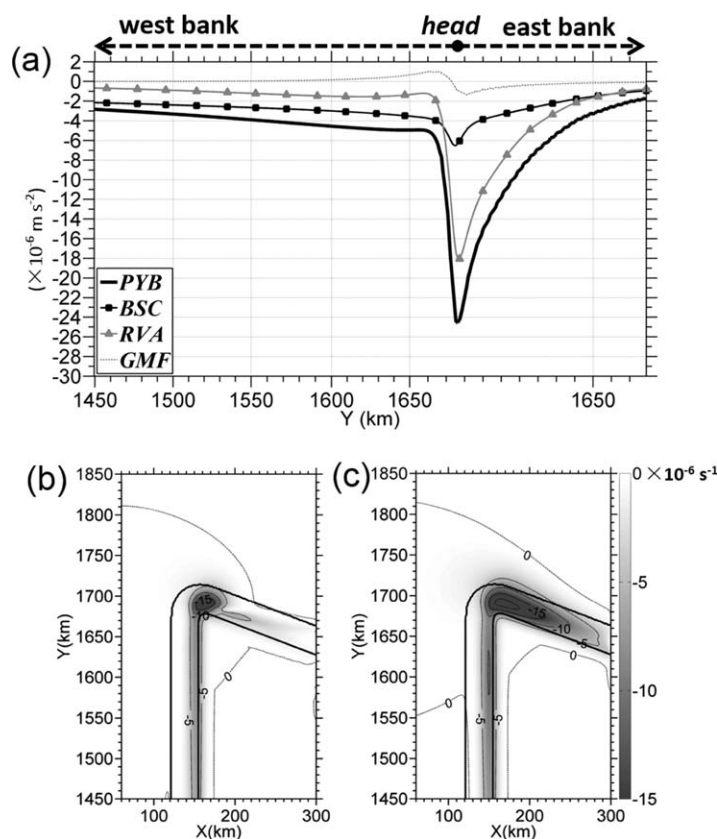


Figure 16. (a) Terms (m s^{-2}) in the depth-integrated vorticity equation (3) along the 50 m isobath, and horizontal maps of depth-averaged relative vorticity (ζ , 10^{-6} s^{-1}) from (b) the standard case and (c) the sensitivity experiment with enlarged wind stress.

that the frictional effects on the PGF_s are important in all scenarios over the ECS shelf and might play a role over other valleys on the continental shelves in the world's ocean.

6. Summary and Conclusion

We used observations and numerical model simulations to investigate the distinct upwelling process and the underlying dynamics over the submerged valley on the ECS shelf. The numerical simulation with a realistic ECS shelf topography reproduced the observed upwelling features over the valley very well. The simulation revealed that an intensified upslope transport of cold deep water over the unique topography of the valley caused the upwelling. The transport existed prominently along the west bank on the seaside of the coastal current and peaked around the valley's head. No similar upslope transport was found along the east bank. A distinct high-pressure center was formed downstream of the valley because of the anticyclonic circulation over the valley. The anticyclonic circulation was resulted from the vertical squeezing of vortex tube or nonlinear vorticity advection when the current flowed over the valley.

We established the forcing mechanism of the upwelling by conducting analyses of momentum and vorticity balances based on a conceptual simulation with idealized topography. We found that a negative along-bank PGF_s geostrophically induced the upslope cross-bank geostrophic transport. This led to the intensified upwelling along the west bank and around the head of the valley. The negative PGF_s along the west bank increased downstream and peaked near the head.

Although PGF_s has been well recognized as the main force driving the upwelling over a topographic valley, the origin of PGF_s is not well understood in many historic studies. The relative roles of nonlinearity and frictional effects in PGF_s have not been adequately discussed. Using depth-integrated vorticity dynamics, we identified the bottom stress curl as the origin of the PGF_s along the west bank. However, near the head, the

transport along the east bank, especially when the coastal current was strong and/or the valley was relatively deep. Under this condition, the non-linear advection associated with the vertical squeezing of the vortex tube over the canyon substantially boosted PGF_s at the downstream rim and led to a considerable upslope current.

However, it is important to note that as a result of increased curvature vorticity on the east bank around the head, BSC also increased (Figure 16a). BSC 's contribution to PGF_s along this part of the east bank was actually comparable to that of RVA over the slope between the 30 m and 50 m isobaths, where vorticity due to the vertical squeezing of vortex tube was the greatest (Figure 16c). Clearly, the radius of curvature of the valley determined the magnitude of curvature vorticity for RVA as in *Allen and Hickey* [2010]. We showed

contributions of both the bottom stress curl and the vorticity advection amplified, with the latter dominating the former. Both peaked at the head of the valley. The negative shear vorticity on the seaside of the upwelling current was the source of the bottom stress curl along the west bank. The curvature vorticity due to vertical squeezing of the vortex tube around the head was the source of the bottom stress curl around the head.

We demonstrated that when the wind-driven current, and, thus, nonlinearity strengthened, the robust upwelling dynamics prevailed. However, we found that the upslope cross-bank transport and upwelling also occurred near the head along the east bank as well, as the current over the valley grew stronger. The PGF_s and the bottom friction mainly generated this cross-bank transport. The PGF_s was due to the strengthened vorticity advection along the east bank around the head. The bottom frictional effects were due to locally increased negative curvature vorticity.

The results of our study suggest that the commonly observed upwelling over the topographic valley on the continental shelf is the result of cross-isobath geostrophic transport associated with both nonlinear (or vertical squeezing of the vortex tube) and frictional responses of the flow to the topography. The upwelling occurs as a result of the vertical squeezing of the vortex tube in the downstream rim around the head of the valley, and its magnitude is largely governed by bottom stress curl over the entire valley. The relative importance of nonlinear and frictional effects is determined by the characteristics of the current over the valley and the topography of the valley itself.

Acknowledgments

This research was supported by the National Key Basic Research Development Program 2009CB421208, by Hong Kong's Research Grant Council under project N_HKUST627/13 and by the State Key Laboratory in Marine Pollution (SKLMP) Seed Collaborative Research Fund under project SKLMP/SCRF/0006. The data for this study are available from the corresponding author at e-mail: magan@ust.hk. The authors are grateful for the suggestions and comments provided by two anonymous reviewers.

References

- Allen, S. E. (2000), On subinertial flow in submarine canyons: Effect of geometry, *J. Geophys. Res.*, *105*(C1), 1285–1297, doi:10.1029/1999JC900240.
- Allen, S. E. (2004), Restrictions on deep flow across the shelf-break and the role of submarine canyons in facilitating such flow, *Surv. Geophys.*, *25*(3–4), 221–247, doi:10.1007/s10712-004-1275-0.
- Allen, S. E., and X. D. de Madron (2009), A review of the role of submarine canyons in deep-ocean exchange with the shelf, *Ocean Sci.*, *5*(4), 607–620.
- Allen, S. E., and B. M. Hickey (2010), Dynamics of advection-driven upwelling over a shelf break submarine canyon, *J. Geophys. Res.*, *115*, C08018, doi:10.1029/2009JC005731.
- Allen, S. E., C. Vindeirinho, R. E. Thomson, M. G. G. Foreman, and D. L. Mackas (2001), Physical and biological processes over a submarine canyon during an upwelling event, *Can. J. Fish. Aquat. Sci.*, *58*(4), 671–684, doi:10.1139/cjfas-58-4-671.
- Chu, P., Y. C. Chen, and A. Kuninaka (2005), Seasonal variability of the Yellow Sea/East China Sea surface fluxes and thermohaline structure, *Adv. Atmos. Sci.*, *22*(1), 1–20, doi:10.1007/Bf02930865.
- Dawe, J. T., and S. E. Allen (2010), Solution convergence of flow over steep topography in a numerical model of canyon upwelling, *J. Geophys. Res.*, *115*, C05008, doi:10.1029/2009JC005597.
- Flexas, M. M., D. L. Boyer, M. Espino, J. Puigdefabregas, A. Rubio, and J. B. Company (2008), Circulation over a submarine canyon in the NW Mediterranean, *J. Geophys. Res.*, *113*, C12002, doi:10.1029/2006JC003998.
- Freeland, H. J., and K. L. Denman (1982), A Topographically Controlled Upwelling Center Off Southern Vancouver Island, *J. Mar. Res.*, *40*(4), 1069–1093.
- Gan, J. P., and J. S. Allen (2002), A modeling study of shelf circulation off northern California in the region of the Coastal Ocean Dynamics Experiment: Response to relaxation of upwelling, *J. Geophys. Res.*, *107*(C9), 3123, doi:10.1029/2000JC000768.
- Gan, J. P., and J. S. Allen (2005), On open boundary conditions for a limited-area coastal model off Oregon. Part 1: Response to idealized wind forcing, *Ocean Modell.*, *8*(1–2), 115–133, doi:10.1016/j.ocemod.2003.12.006.
- Gan, J. P., J. S. Allen, and R. M. Samelson (2005), On open boundary conditions for a limited-area coastal model off Oregon. Part 2: Response to wind forcing from a regional mesoscale atmospheric model, *Ocean Modell.*, *8*(1–2), 155–173, doi:10.1016/j.ocemod.2003.12.007.
- Gan, J. P., A. Cheung, X. G. Guo, and L. Li (2009), Intensified upwelling over a widened shelf in the northeastern South China Sea, *J. Geophys. Res.*, *114*, C09019, doi:10.1029/2007JC004660.
- Gan, J. P., H. S. Ho, and L. L. Liang (2013), Dynamics of intensified downwelling circulation over a widened shelf in the northeastern South China Sea, *J. Phys. Oceanogr.*, *43*(1), 80–94, doi:10.1175/Jpo-D-12-02.1.
- Haidvogel, D. B. (2005), Cross-shelf exchange driven by oscillatory barotropic currents at an idealized coastal canyon, *J. Phys. Oceanogr.*, *35*(6), 1054–1067, doi:10.1175/Jpo2735.1.
- Hickey, B. (1995), *Coastal submarine canyons, Topographic Effects in the Ocean, SOEST Spec. Publ.*, pp. 95–110, Sch. of Ocean and Earth Sci. and Technol., Honolulu, Hawaii.
- Hickey, B. (1997), The response of a steep-sided, narrow canyon to time-variable wind forcing, *J. Phys. Oceanogr.*, *27*(5), 697–726, doi:10.1175/1520-0485(1997)027<0697:Troass>2.0.Co;2.
- Kämpf, J. (2006), Transient wind-driven upwelling in a submarine canyon: A process-oriented modeling study, *J. Geophys. Res.*, *111*, C11011, doi:10.1029/2006JC003497.
- Kämpf, J. (2007), On the magnitude of upwelling fluxes in shelf-break canyons, *Cont. Shelf Res.*, *27*(17), 2211–2223, doi:10.1016/j.csr.2007.05.010.
- Klinck, J. M. (1996), Circulation near submarine canyons: A modeling study, *J. Geophys. Res.*, *101*(C1), 1211–1223.
- Li, X. X., T. S. Bianchi, Z. S. Yang, L. E. Osterman, M. A. Allison, S. F. DiMarco, and G. P. Yang (2011), Historical trends of hypoxia in Changjiang River estuary: Applications of chemical biomarkers and microfossils, *J. Mar. Syst.*, *86*(3–4), 57–68, doi:10.1016/j.jmarsys.2011.02.003.
- Liu, Z. Q., and J. P. Gan (2014), Modeling study of variable upwelling circulation in the East China Sea: Response to a coastal promontory, *J. Phys. Oceanogr.*, *44*(4), 1078–1094, doi:10.1175/Jpo-D-13-0170.1.

- Lü, X., F. Qiao, C. Xia, J. Zhu, and Y. Yuan (2006), Upwelling off Yangtze River estuary in summer, *J. Geophys. Res.*, *111*, C11S08, doi:10.1029/2005JC003250.
- Lü, X., F. Qiao, C. Xia, and Y. Yuan (2007), Tidally induced upwelling off Yangtze River estuary and in Zhejiang coastal waters in summer, *Sci. China Ser. D Earth Sci.*, *50*(3), 462–473, doi:10.1007/s11430-007-2050-0.
- Marchesiello, P., J. C. McWilliams, and A. Shchepetkin (2001), Open boundary conditions for long-term integration of regional oceanic models, *Ocean Modell.*, *3*(1–2), 1–20, doi:10.1016/S1463-5003(00)00013-5.
- Mellor, G. L., and T. Yamada (1982), Development of a turbulence closure-model for geophysical fluid problems, *Rev. Geophys.*, *20*(4), 851–875, doi:10.1029/RG020i004p00851.
- Qiao, F. L., Y. Z. Yang, X. G. Lv, C. S. Xia, X. Y. Chen, B. D. Wang, and Y. L. Yuan (2006), Coastal upwelling in the East China Sea in winter, *J. Geophys. Res.*, *111*, C11S06, doi:10.1029/2005JC003264.
- Shchepetkin, A. F., and J. C. McWilliams (2005), The regional oceanic modeling system (ROMS): A split-explicit, free-surface, topography-following-coordinate oceanic model, *Ocean Modell.*, *9*(4), 347–404, doi:10.1016/j.ocemod.2004.08.002.
- Song, Y., and D. Haidvogel (1994), A semi-implicit ocean circulation model using a generalized topography-following coordinate system, *J. Comput. Phys.*, *115*, 228–244.
- Song, Y. T., D. B. Haidvogel, and S. M. Glenn (2001), Effects of topographic variability on the formation of upwelling centers off New Jersey: A theoretical model, *J. Geophys. Res.*, *106*(C5), 9223–9240, doi:10.1029/2000JC000244.
- Springer, S. R., R. M. Samelson, J. S. Allen, G. D. Egbert, A. L. Kurapov, R. N. Miller, and J. C. Kindle (2009), A nested grid model of the Oregon Coastal Transition Zone: Simulations and comparisons with observations during the 2001 upwelling season, *J. Geophys. Res.*, *114*, C02010, doi:10.1029/2008JC004863.
- Wang, B. (2009), Hydromorphological mechanisms leading to hypoxia off the Changjiang estuary, *Mar. Environ. Res.*, *67*, 53–58, doi:10.1016/j.marenvres.2008.11.001.
- Waterhouse, A. F., S. E. Allen, and A. W. Bowie (2009), Upwelling flow dynamics in long canyons at low Rossby number, *J. Geophys. Res.*, *114*, C05004, doi:10.1029/2008JC004956.
- Wei, H., Y. C. He, Q. J. Li, Z. Y. Liu, and H. T. Wang (2007), Summer hypoxia adjacent to the Changjiang Estuary, *J. Mar. Syst.*, *67*(3–4), 292–303, doi:10.1016/j.jmarsys.2006.04.014.
- Whitney, M. M., and J. S. Allen (2009), Coastal wind-driven circulation in the vicinity of a bank. Part I: Modeling flow over idealized symmetric banks, *J. Phys. Oceanogr.*, *39*(6), 1273–1297, doi:10.1175/2008jpo3966.1.
- Yang, D. Z., B. S. Yin, Z. L. Liu, T. Bai, J. F. Qi, and H. Y. Chen (2012), Numerical study on the pattern and origins of Kuroshio branches in the bottom water of southern East China Sea in summer, *J. Geophys. Res.*, *117*, C02014, doi:10.1029/2011JC007528.
- Zhao, B. R. (1982), A study of the effects of local wind on currents in the off-shore areas of the East China Sea and Huanghai Sea, *Oceanol. Limnol. Sin.*, *6*, 479–490.
- Zhao, B. R. (1993), Upwelling phenomenon off Changjiang estuary, *Acta Oceanol. Sin.*, *15*, 106–114.